Available online at www.sciencedirect.com
SCIENCE DIRECT
ELSEVIER
Ultramicroscopy 106 (2006) 822–828
ultramicroscopy
www.elsevier.com/locate/ultramic

Improving the contrast of topographical AFM images by a simple averaging filter

F. Kienberger[a,*], V.P. Pastushenko[a], G. Kada[b], T. Puntheeranurak[a], L. Chtcheglova[a], C. Riethmueller[c], C. Rankl[a], A. Ebner[a], P. Hinterdorfer[a]

[a]*Institute for Biophysics, Johannes Kepler University of Linz, Altenbergerstrasse 69, A-4040 Linz, Austria*
[b]*Molecular Imaging Corporation, 4666 S. Ash Avenue, Tempe, AZ 85282, USA*
[c]*Nanolab, Institute of Physiology II, University of Münster, Münster D-48149, Germany*

Received 11 August 2005; accepted 17 November 2005

Abstract

New image-processing methods were applied to atomic force microscopy images in order to visualize small details on the surface of virus particles and living cells. Polynomial line flattening and plane fitting of topographical images were performed as first step of the image processing. In a second step, a sliding window approach was used for low-pass filtering and data smoothing. The size of the filtering window was adjusted to the size of the small details of interest. Subtraction of the smoothed data from the original data resulted in images with enhanced contrast. Topographical features which are usually not visible can be easily discerned in the processed images. The method developed in this study rendered possible the detection of small patterns on viral particles as well as thin cytoskeleton fibers of living cells. It is shown that the sliding window approach gives better results than Fourier-filtering. Our method can be generally applied to increase the contrast of topographical images, especially when small features are to be highlighted on relatively high objects.

Keywords: Image processing; Contrast enhancement; Atomic force microscope; Virus; Cells

1. Introduction

At present, atomic force microscopy (AFM) is extensively used in the wide range of disciplines such as biology, solid-state physics and materials science to image surfaces on scales from micro- to nanometer with the objective to visualize and properly characterize surface textures and shapes [1]. For instance, it has been applied to characterize various biological samples (e.g. proteins, DNA, membranes, cells, etc.) at high lateral resolution [2]. Moreover, it is the only technique that provides sub-nanometer resolution at an outstanding signal-to-noise ratio under physiological conditions. Due to continuous developments of sample preparation, imaging techniques and instrumentation, AFM has been emerged as a complementary technique to X-ray crystallography and electron microscopy (EM) for the determination of the structure of various proteins [3,4].

In its application to viruses and virus-related processes, AFM has successfully complemented EM and X-ray diffraction studies [5,6]. With AFM, virus particles can be visualized in appropriate buffers that preserve structure over extended periods of time. Most importantly, AFM does not rely on symmetry averaging and crystallization. Thus, AFM can reveal defects and structural anomalies of individual virus particles. AFM yields three-dimensional images and, unlike transmission EM, not projections of particles onto a plane. In contrast to EM, the resolution of AFM is very good in the vertical direction (less than a nanometer). Recently, AFM studies gave new insights into the architecture of various isolated viruses [7]. In the application of AFM to living cells, new cellular surface structures and their physiological functions have been revealed [8–10]. For instance, topographical images of

*Corresponding author. Tel.: +43 732 2468 9265; fax: +43 732 2468 9270.
E-mail address: ferry.kienberger@jku.at (F. Kienberger).

0304-3991/$ - see front matter © 2006 Elsevier B.V. All rights reserved.
doi:10.1016/j.ultramic.2005.11.013

living pancreatic acinar cells revealed the presence of fusion pores at the apical plasma membrane, as well as its structure and dynamics. This work highlighted for the first time pit-like structures containing typically three or four depressions with the size of about 150 nm [8]. In another study, topographical imaging could show processes induced by viral infection of living cells [11]. Human immunodeficiency virions were thereby imaged on lymphocytes at high resolution and considerable details of the virus-cell arrangement were obtained. However, imaging of living cells can be somewhat complicated by the fact that cells are relatively soft and fragile, and thus the typical applied forces during scanning can distort or permanently destroy such structures [12]. As a consequence, the resolution of AFM images of cells was limited to 10 nm so far [13,14].

The aim of this study is to properly visualize small features (e.g. cytoskeleton structures with some nanometers in height) on relatively high objects (e.g. the cell nuclei with several micrometers in height). The contrast of topographical images is usually adjusted by changing the scale in vertical direction. However, by applying this simple strategy, it is only possible to highlight either the lower or the higher parts of the image [15]. Here, we developed an image-processing method that allows visualizing low and high topographical features simultaneously. The contrast of the images is thereby significantly improved, as illustrated by AFM images of viruses and living cells.

2. Materials and methods

2.1. Human rhinoviruses (HRV)

HRV2, originally obtained from the American Type Culture Collection (ATCC), was prepared in HeLa-H1 cells grown in suspension culture and purified by sucrose density gradient centrifugation. A detailed protocol for the isolation of HRV2 particles is given in Ref. [16]. Ten microliters of ~1 mg/ml HRV2 in 50 mM Tris buffer containing 5 mM $NiCl_2$ (pH 7.6) were deposited on freshly cleaved mica for 15 min resulting in a densely packed HRV2 monolayer. A lower coverage of the surface was obtained by reducing the HRV2 concentration. Unattached viruses were removed by washing three times with the same buffer and imaging was done in 50 mM Tris, 5 mM $NiCl_2$ (pH 7.6).

2.2. Cell culture

Two cell types were used in this study, chinese hamster ovary (CHO) cells (Fig. 2) and microvascular endothelial cell line from mouse myocardium (MyEnd) (Fig. 3) [17]. Parental CHO cells were obtained from the ATCC. CHO cells were grown in 25 cm^2 flasks under 5% CO_2 at 37 °C. These cells were cultured in Dulbecco's modified Eagle's medium (DMEM), containing high glucose (25 mM) supplemented with 5% fetal calf serum (FCS), 1 mM sodium pyruvate, 2 mM L-glutamine, 1x minimal essential medium (MEM) and 25 μM β-mercaptoethanol. Culture medium was renewed three times a week and the cells were subcultured at 80% confluence. Cell passages below 15 were used for all experiments. MyEnd cells were grown in DMEM medium supplemented with 10% FCS and antibiotics (penicillin, streptomycin) in a humidified atmosphere (95% air, 5% CO_2) at 37 °C as described in Ref. [18].

2.3. AFM imaging

Topographical images of HRV were acquired in a buffer solution in intermittent contact mode with a magnetically driven AFM (MACmode, Molecular Imaging, Tempe, AZ) using magnetically coated MacLevers (Molecular Imaging, Tempe, AZ). Amplitude-distance cycles were used to adjust the free cantilever oscillation amplitude to 5–15 nm and to determine the optimal amplitude reduction value (i.e. the set point) to 10–30%. Both the low value of the free oscillation amplitude and the low amplitude reduction used as feedback signal are of particular importance for preventing disruption of the sample and stable imaging. The oscillation frequency was adjusted to ~7 kHz using the resonance curve and the related phase response curve. The cantilevers for MACmode imaging had a spring constant of 0.1 N/m, as calibrated in solution using the equipartition principle [19]. Images were taken at a line scan rate of ~1 Hz and 512 pixels per line were recorded. Image acquisition time was thus of about 9 min.

CHO cells were seeded on 22 mm^2 poly-L-lysine-coated glass cover slips and the experiments were performed within 1–4 days of seeding the cover slips. Topographical images of CHO cells (Fig. 2(d)) were acquired with contact mode AFM in the Krebs–Ringer-HEPES-Na (KRH-Na) medium at room temperature with 0.1 N/m spring constant cantilevers (Veeco, Germany). The KRH-Na medium contained in mM: 120 NaCl, 4.7 KCl, 2.2 $CaCl_2$, 1.2 $MgCl_2$ and 10 HEPES, pH 7.4. MyEnd cells were seeded onto 0.5% gelatine-coated glass slides and examined in 50% confluent state (Fig. 3). Topographical images of MyEnd cells were acquired with contact mode AFM in Hanks' balanced salt solution (HBSS) containing 1.26 mM Ca^{2+} with 0.03 N/m spring constant cantilevers at room temperature.

2.4. Image processing

The surface area of the images varied from $70 \times 70\,nm^2$ to $85 \times 85\,\mu m^2$ with heights ranging from 2 nm to 5 μm. Images are represented either by a 512×512 or 256×256 matrix. Topographical images (raw data without flattening) obtained by AFM were used as initial data. For line-wise flattening, plane fitting and contrast enhancement, the data were imported into MATLAB Version 7 (MathWorks Inc., Natick, MA). All programs used in this work are

posted on MATLAB file-exchange (http://www.mathworks.com/matlabcentral/fileexchange). The first step in contrast enhancement was planar tilting of the raw images. A smoothed image was then calculated using SAVFILT (Simply AVeraging FILTer for vectors or matrices), a generalized and improved version of the Savitzky–Golay filter; a detailed description of the Savitzky–Golay filter, which is a standard tool in MATLAB, is given in Ref. [20]. In comparison, SAVFILT results in a better processing at the boundaries of the image. Instead of replacing the data points at the edges of the image by corresponding polynomial values, a maximally sized, symmetric frame is used in SAVFILT. In addition, SAVFILT accepts an arbitrary window size (including any non-integer value), in contrast to the Savitzky–Golay filter which only allows odd values. For odd window sizes, the results of both approaches are identical in internal points of the image. For Fig. 2(b), SAVFILT was used with a window size of 35 pixels; for Figs. 2(e) and 3, a window with 70 pixels was used. The level of filtering was chosen in such a way that the smoothed image does not show any details of the substructures of interest. This was also done with Fourier-filtering and standard Savitzky–Golay filter by selecting a cut-off frequency for Fourier-filtering (Fig. 4), or by selecting an appropriate window size for Savitzky–Golay filtering. Only frequencies lower than the cut-off frequency were retained in the Fourier-image (Fig. 4(a)). The amplitudes for higher frequencies were weighted exponentially. For Fig. 4(a), 22 frequencies were retained (positive and negative values together) out of 512 frequencies (the image size was 512×512 pixels). For Fig. 4(b), the window size was varied from 3 to 100 pixels (Savitzky–Golay and SAVFILT), and the number of retained frequencies from 3 to 100 (Fourier).

3. Results and discussion

3.1. Image flattening

Usually, the first step in processing AFM images is line-wise flattening to remove inevitable artifacts of the image acquisition process [21]. For instance, it is unlikely that a sample is exactly perpendicular to the AFM tip, resulting in some tilt that is not representative for the sample surface. Other sources of artifacts come from vertical scanner drift, image bow due to scanner non-linearities, line skips, etc. Thus, polynomial flattening procedures are normally used to remove the offset on a line-by-line basis [22]. The polynomial order can thereby range from zero to usually four. Since the polynomial order of the fit determines the number of zero points per line, second-order polynomials can, as a simple rule of thumb, correct for artifacts ranging one-half of the image size, third-order polynomials can correct for one-third of the image size, and so on. Another method to remove scanning acquisition artifacts is plane fitting, where a plane is removed from the scan that had been least-squares fitted to all rows of data. The plane fitting is preferentially done with first-order, i.e. planar tilting.

Although polynomial flattening can minimize height artifacts on smooth surfaces, further artifacts are introduced when images with high features are processed [23]. Fig. 1(a) compares line-wise flattening with planar tilting on images of viral particles on mica surface. Virions appear in AFM images as objects of about 30 nm in height, as determined from the cross-section profile using mica as reference [16]. Due to the low z-scale (ranging from 0 to 2 nm), viral particles are seen uniformly as bright spots; a three-dimensional presentation at full z-scale (ranging from 0 to 30 nm) is shown as inset in Fig. 1(a). Using a third-order polynomial for flattening, black bands surround the viral particles on the fast scan axis (Fig. 1(a), left panel). In addition, artificial bright spots appear at the end of the

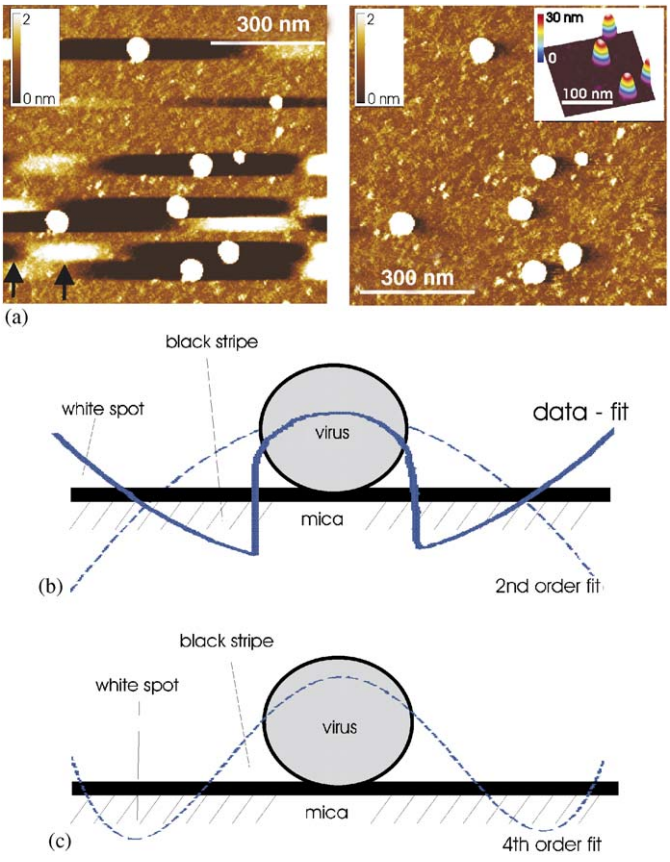

Fig. 1. Polynomial flattening and corresponding artifacts. (a) Left panel: topographical image of single rhinovirus particles flattened using third-order polynomials. Individual virus particles on mica were observed as white spots with 30 nm in height. Flattening results in artifacts on the fast scan axis. The scan size was $900 \times 900\,nm^2$. The z-scale ranges from 0 to 2 nm. Right panel: the same image was planar tilted. Artificial features are not present. Scan size and z-scale are the same as before. The inset shows a three-dimensional representation of the viral particles. (b) A second-order polynomial (dashed line) was fitted to a single, spherical particle (e.g. virus) on a flat surface (e.g. mica). The difference between the surface relief and the polynomial fit (solid line) shows negative and positive values (corresponding to black bands and white spots, respectively). (c) A fourth-order polynomial was fitted to the same relief (dashed line), resulting in periodic artifacts along the fast scan line.

black bands. These artifacts are not observed in the planar tilted image (Fig. 1(a), right panel). When small objects are in close proximity to viral particles, flattening artifacts (i.e. black bands) can make their detection difficult [24]. The artificial features are located at certain positions, depending on the polynomial order used. In the flattening process, a least-square fit is calculated for each scan line (Fig. 1(b), dashed line). The polynomial fit is then subtracted from the corresponding scan line (Fig. 1(b), solid line), resulting in negative values close to the virus particles (black bands) followed by positive values (white features). For third- and higher order polynomial flattening, black strips and white features appear alternating in the flattened scan line (Fig. 1(c)). Alternating black and white features can also be observed in Fig. 1(a) (arrows).

3.2. Contrast enhancement

The presentation of small features on large objects is a frequently occurring task in the investigation of biological samples. For instance, in a previous study, we imaged symmetrically arranged protrusions on 30-nm-sized virus particles [25]. Since the height of the protrusions is only ~0.5 nm, image processing was necessary to make them easily visible. In the following, we give a detailed account of the image processing used in Ref. [25]. Furthermore, the same method is applied to images of living cells.

Fig. 2(a) shows a densely packed monolayer of viral particles on a mica surface. The height of the virus layer was determined to be ~30 nm from the cross-section profile using an uncovered spot on mica as reference. The tight packing and close apposition of the virions result in some structural deformation of the virus capsid [26]. A regularly spaced pattern of ~20 protrusions with ~2 nm in diameter and ~0.5 nm in height can be weakly observed on almost all viral particles (Fig. 2(a)). This pattern reflects the protrusions on the surface of viral capsids known from cryo-EM and X-ray crystallography [27]. To improve the visibility of the pattern, a digital smoothing filter (SAVFILT, cf. Section 2) was applied. A sliding window of adjustable size was used to calculate a smoothed image from the original image (Fig. 2(b)) [28]. For each pixel, an average value is computed on the basis of its surrounding pixels in both directions. The smoothed image was then subtracted from the original image, resulting in a clearer presentation of the smaller elevations on top of the viral particles (Fig. 2(c)). Many features are discernable in the contrast-enhanced image (Fig. 2(c)). For example, the number of protrusions can be investigated on each viral particle, as well as their arrangement; a detailed analysis is given in Ref. [25]. Protrusions on the edge of the virus capsid can be observed which are not discernable in the original image. Overall, viral particles did not appear strictly globular in shape, but rather the projection of the particles represented some straight borders akin to their polygonal surface features that were also observed by cryo-EM [27].

The same method can be applied to AFM images obtained on much more higher objects such as living cells. Fig. 2(d) shows a topographical image of living CHO cells

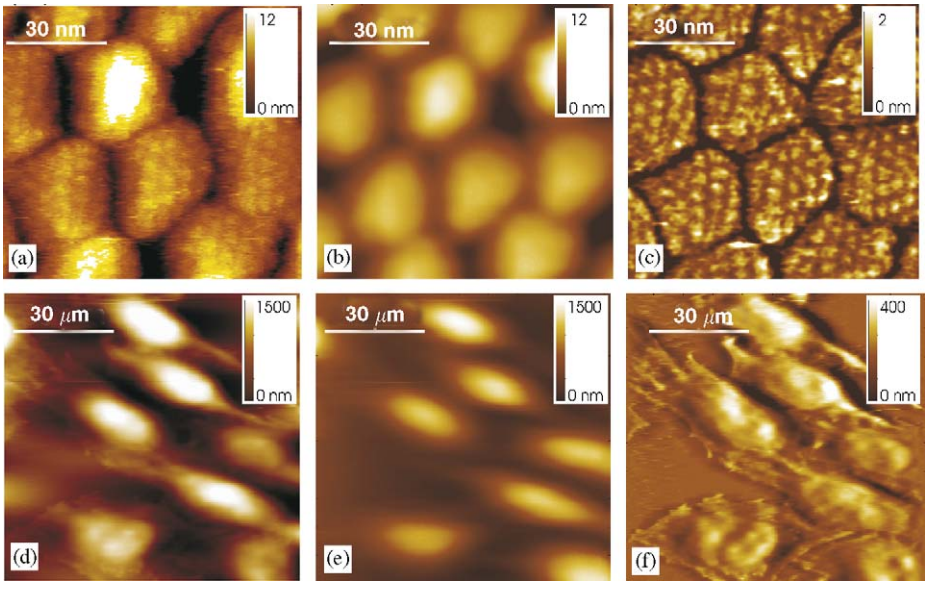

Fig. 2. Contrast enhancement of topographical images of viral particles and living cells. (a) Dense packing of virus particles. A regular pattern of small protrusions with ~0.5 nm in height can be weakly discerned on the viral capsids. The scan size was $75 \times 75\,nm^2$. The z-scale ranges from 0 to 12 nm. (b) Smoothed image calculated with SAVFILT. Scan size and z-scale are the same as before. (c) Contrast-enhanced image. Subtraction of the smoothed image from the original image results in a much clearer presentation of the protrusions. The z-scale ranges from 0 to 2 nm. (d) Topographical image of living CHO cells. Cells are about 30 μm in diameter and ~3 μm in height. Flat regions surrounding the nucleus area are only ~300 nm in height. The scan size was $75 \times 75\,\mu m^2$. The z-scale ranges from 0 to 1.5 μm. (e) Smoothed image calculated with SAVFILT. Scan size and z-scale are the same as before. (f) Contrast-enhanced image. Subtraction of the smoothed image from the original image results in a much clearer presentation of the lower parts of the cells. The z-scale ranges from 0 to 400 nm.

at $75 \times 75\,\mu m^2$ scan size. Typical CHO cells are 30–70 μm in diameter with a characteristic bright zone corresponding to the nucleus area with 2–4 μm in height. The flat region that surrounds the nucleus represents the expansion of the cells, which assists for cell adhesion and communication with neighboring cells; the dominant features are thereby cytoskeleton structures. Using the same image-processing method as before, a smoothed image was calculated (Fig. 2(e)) and subtracted from the original image. The contrast-enhanced image (Fig. 2(f)) reveals details of both the cell nucleus and the flat regions surrounding the nucleus. A topographical image of a single endothelial cell is shown in Fig. 3(a). The contrast-enhanced image (Fig. 3(b)) shows details of the cytoskeleton arrangement on both the nuclei and the surrounding flat regions. Reducing the scan size further, smaller cytoskeleton structures can be observed (Fig. 3(c)). Some cytoskeleton features are visible in the original image; however, much more details are obtained in the contrast-enhanced image (Fig. 3(d)). Globular and filamentous cytoskeleton structures are clearly resolved in the processed image with roughly 10 nm in height (Fig. 3(d), arrow), structures that cannot be observed in the original image [18].

3.3. Comparison of SAVFILT, Savitzky–Golay filter, and Fourier-filter

In the following, we compare three different filters for the purpose of contrast enhancement. Fourier-filtering, first-order Savitzky–Golay filter and SAVFILT (cf. Section 2) were used to calculate the smoothed image from the same original image (Fig. 2(a)). This was achieved by selecting a cut-off frequency for the Fourier-method, and by selecting an appropriate window size for Savitzky–Golay and SAVFILT methods. Contrast-enhanced images were calculated by subtracting the smoothed images from the original image; the results are shown in Fig. 4. SAVFILT (Fig. 2(c)) and Savitzky–Golay filter (not shown) generally show very similar results and only minor differences were observed at the edges of the images. The Fourier-filtered image (Fig. 4(a)), however, shows many artifacts at the edges (white and black features; see arrows).

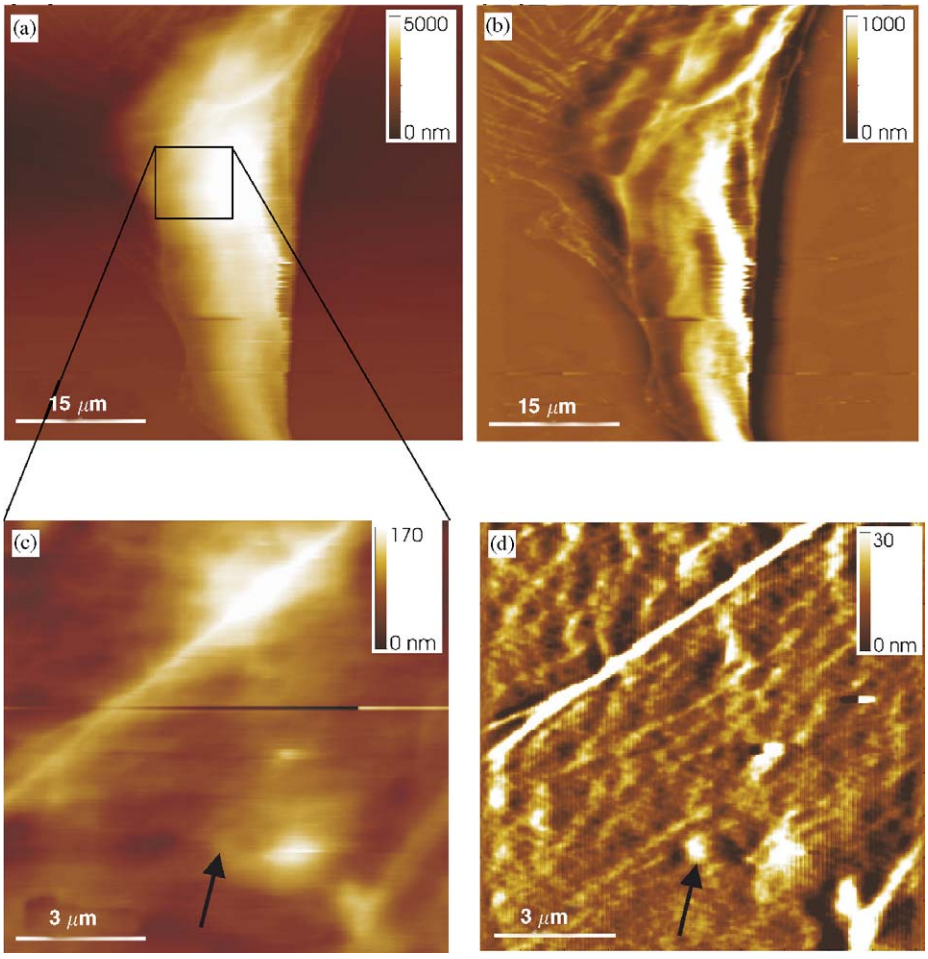

Fig. 3. Contrast enhancement of a single cell image. (a) Overview image of a living MyEnd cell. The nucleus region is surrounded by flat cytoskeleton areas. The scan size was $50 \times 50\,\mu m^2$. The z-scale ranges from 0 to 5 μm. (b) Contrast-enhanced image (same processing as in Fig. 2; smoothed image not shown) shows tiny features both on the flat regions and on the nucleus. The z-scale ranges from 0 to 1 μm. (c) Smaller scan area on the cell surface exhibiting cytoskeleton features. The scan size was $12 \times 12\,\mu m^2$. The z-scale ranges from 0 to 170 nm. (d) The contrast-enhanced image shows fine details of the cell surface that are not discernable in the original image (arrow). The z-scale ranges from 0 to 30 nm.

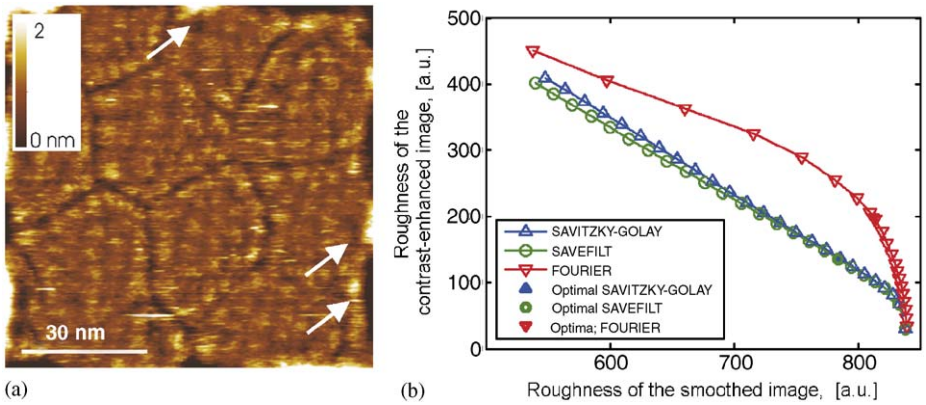

Fig. 4. Comparing different methods for contrast enhancement. (a) Using Fourier-filtering, a smoothed image (not shown) was calculated from the original image (Fig. 2(a)), and subtraction resulted in the contrast-enhanced image shown. Arrows point to artifacts introduced by Fourier-filtering. Scan size and z-scale are the same as in Fig. 2(c). (b) Comparison of the performance of Fourier-filtering, Savitzky–Golay filter and SAVFILT using the same original image Fig. 2(a). At a given roughness (i.e. variance) of the smoothed image, SAVFILT shows the lowest roughness of the contrast-enhanced image.

The overall contrast of the Fourier-filtered image is weaker as evident by the blurred boundaries of virus particles compared to the sharp boundaries in the SAVFILT image (Fig. 2(c)).

To compare the results quantitatively, we have plotted the roughness (i.e. the variance of the topographical data) of the contrast-enhanced image versus the roughness of the smoothed image, calculated at different cut-off frequencies (Fourier) and at different sizes of the filtering window (Savitzky–Golay and SAVFILT) (Fig. 4(b)). This type of comparison is based on the fact that the variance is a sufficiently robust property of topographical images, and is clearly related to the aim of increasing the visibility of the small features (e.g. protrusions on the virus) by subtracting the profiles of the large objects (e.g. the virus itself). A lower variance of the contrast-enhanced image corresponds therefore to a better performance of the filtering method. From Fig. 4(b), one can see that at a given roughness of the smoothed image, the Fourier-image shows a remarkably larger roughness of the contrast-enhanced image than the window-based images. In the whole range of window-sizes, SAVFILT shows a slightly better performance (i.e. a lower variance of the contrast-enhanced image) than the Savitzky–Golay filter.

The main advantage of using a sliding window approach for low-pass filtering is that no artifacts are introduced; simple averaging in real-space is the only operation executed. Furthermore, it operates only within the preset window size. Therefore, artifacts already present in the original image (jumps in scan lines, large spots of dirt, etc.) do not propagate over the whole data set, but influence only the pixels within the window. The window size can be set several times larger than the lateral size of the small features (e.g. protrusions on the virus). This guarantees that local heights of the small features are preserved, as evident from the comparison of heights before (i.e. original image) and after image processing (i.e. contrast-enhanced image). The height information of the large objects (e.g. the virus itself) is completely separated from the small features and can be simply obtained from the smoothed image.

4. Conclusion

In this work, we presented an easy and robust procedure for the improvement of the contrast of topographical AFM images. Line-wise polynomial flattening, which is usually applied in the first step of image processing, causes artificial black bands and white features when images with relatively large objects are processed. These artifacts are not present on planar tilted images. A simple sliding window approach (SAVFILT) was used to calculate a smoothed image from the original one, and its subtraction resulted in contrast-enhanced images. Thereby, small features which are usually not discernable can be easily observed, as exemplified on virus and cell images. This method can be applied to any AFM images where small features are to be highlighted on relatively large objects. The main advantage of this window-based approach over Fourier-methods is that the former acts locally, therefore better reflecting the slowly varying components of the surface. In contrast, the amplitude of every frequency of the Fourier-spectrum is influenced by the whole image and their different artifacts.

Acknowledgments

This work was supported by Austrian Science Foundation projects P14549, the Human Frontier Science Program (RG-P0053/2004) and the European Commission (STREP program).

References

[1] G. Binnig, C.F. Quate, C. Gerber, Atomic force microscope, Phys. Rev. Lett. 56 (9) (1986) 930–933.
[2] J.K. Horber, M.J. Miles, Scanning probe evolution in biology, Science 302 (5647) (2003) 1002–1005.

[3] D.J. Muller, H. Janovjak, T. Lehto, L. Kuerschner, K. Anderson, Observing structure, function and assembly of single proteins by AFM, Prog. Biophys. Mol. Biol. 79 (1-3) (2002) 1–43.
[4] S. Scheuring, D. Levy, J.L. Rigaud, Watching the components of photosynthetic bacterial membranes and their in situ organisation by atomic force microscopy, Biochim. Biophys. Acta 1712 (2) (2005) 109–127.
[5] Y.G. Kuznetsov, S. Daijogo, J. Zhou, B.L. Semler, A. McPherson, Atomic force microscopy analysis of icosahedral virus RNA, J. Mol. Biol. 347 (1) (2005) 41–52.
[6] Y.G. Kuznetsov, J.R. Gurnon, J.L. Van Etten, A. McPherson, Atomic force microscopy investigation of a chlorella virus, PBCV-1, J. Struct. Biol. 149 (3) (2005) 256–263.
[7] Y.G. Kuznetsov, A.J. Malkin, R.W. Lucas, M. Plomp, A. McPherson, Imaging of viruses by atomic force microscopy, J. Gen. Virol. 82 (Pt 9) (2001) 2025–2034.
[8] A. Jeremic, M. Kelly, S.J. Cho, M.H. Stromer, B.P. Jena, Reconstituted fusion pore, Biophys. J. 85 (3) (2003) 2035–2043.
[9] C.M. Franz, D.J. Muller, Analyzing focal adhesion structure by atomic force microscopy, J. Cell Sci. (2005), in press.
[10] M.S. Zaman, A. Goyal, G.P. Dubey, P.K. Gupta, H. Chandra, T.K. Das, M. Ganguli, Y. Singh, Imaging and analysis of Bacillus anthracis spore germination, Microsc. Res. Tech. 66 (6) (2005) 307–311.
[11] Y.G. Kuznetsov, J.G. Victoria, W.E. Robinson Jr., A. McPherson, Atomic force microscopy investigation of human immunodeficiency virus (HIV) and HIV-infected lymphocytes, J. Virol. 77 (22) (2003) 11896–11909.
[12] V. Vie, M.C. Giocondi, E. Lesniewska, E. Finot, J.P. Goudonnet, C. Le Grimellec, Tapping-mode atomic force microscopy on intact cells: optimal adjustment of tapping conditions by using the deflection signal, Ultramicroscopy 82 (1-4) (2000) 279–288.
[13] C. Le Grimellec, E. Lesniewska, M.C. Giocondi, E. Finot, V. Vie, J.P. Goudonnet, Imaging of the surface of living cells by low-force contact-mode atomic force microscopy, Biophys. J. 75 (2) (1998) 695–703.
[14] F. Kienberger, C. Stroh, G. Kada, R. Moser, W. Baumgartner, V. Pastushenko, C. Rankl, U. Schmidt, H. Muller, E. Orlova, C. LeGrimellec, D. Drenckhahn, D. Blaas, P. Hinterdorfer, Dynamic force microscopy imaging of native membranes, Ultramicroscopy 97 (1-4) (2003) 229–237.
[15] D. Pesen, J.H. Hoh, Micromechanical architecture of the endothelial cell cortex, Biophys. J. 88 (1) (2005) 670–679.
[16] F. Kienberger, R. Zhu, R. Moser, C. Rankl, D. Blaas, P. Hinterdorfer, Dynamic force microscopy for imaging of viruses under physiological conditions, Biol. Proc. Online 6 (2004) 120–128.
[17] N. Golenhofen, W. Ness, E.F. Wawrousek, D. Drenckhahn, Expression and induction of the stress protein alpha-B-crystallin in vascular endothelial cells, Histochem. Cell Biol. 117 (3) (2002) 203–209.
[18] W. Baumgartner, G.J. Schutz, J. Wiegand, N. Golenhofen, D. Drenckhahn, Cadherin function probed by laser tweezer and single molecule fluorescence in vascular endothelial cells, J. Cell Sci. 116 (Pt 6) (2003) 1001–1011.
[19] H.J. Butt, M. Jaschke, Calculation of thermal noise in atomic force microscopy, Nanotechnology 6 (1995) 1–7.
[20] P.H. Eilers, A perfect smoother, Anal. Chem. 75 (14) (2003) 3631–3636.
[21] D. Ricci, P.C. Braga, Recognizing and avoiding artifacts in AFM imaging, Methods Mol. Biol. 242 (2004) 25–37.
[22] J.D. Kiely, D.A. Bonnell, Quantification of topographic structure by scanning probe microscopy, J. Vac. Sci. Technol. B 15 (4) (1997) 1483–1493.
[23] A. Mendez-Vilas, M.L. Gonzalez-Martin, M.J. Nuevo, Optical interference artifacts in contact atomic force microscopy images, Ultramicroscopy 92 (3-4) (2002) 243–250.
[24] F. Kienberger, R. Zhu, R. Moser, D. Blaas, P. Hinterdorfer, Monitoring RNA release from human rhinovirus by dynamic force microscopy, J. Virol. 78 (7) (2004) 3203–3209.
[25] F. Kienberger, C. Rankl, V. Pastushenko, R. Zhu, D. Blaas, P. Hinterdorfer, Visualization of single receptor molecules bound to human rhinovirus under physiological conditions, Structure (Camb) 13 (9) (2005) 1247–1253.
[26] F. Kienberger, R. Moser, H. Schindler, D. Blaas, P. Hinterdorfer, Quasi-crystalline arrangement of human rhinovirus 2 on model membranes, Single Mol. 2 (1) (2001) 99–103.
[27] N. Verdaguer, D. Blaas, I. Fita, Structure of human rhinovirus serotype 2 (HRV2), J. Mol. Biol. 300 (5) (2000) 1179–1194.
[28] M.J.J. Jak, C. Konstapel, A. van Kreuningen, J. Verhoeven, R. van Gastel, J.W.M. Frenken, Automated detection of particles, clusters and islands in scanning probe microscopy images, Surf. Sci. 494 (2001) 43–52.